



RESEARCH ARTICLE

10.1029/2023EA003267

Key Points:

- We present a workflow to reveal segmented fault surfaces within hypocenter distributions through unsupervised learning algorithms
- Comparison with earthquake focal mechanisms corroborates the procedure
- We derive a hierarchical order of planar fault segments associated with different types of faulting

Supporting Information:

Supporting Information may be found in the online version of this article.

Correspondence to:

E. Piegari,
ester.piegari@unina.it

Citation:

Piegari, E., Camanni, G., Mercurio, M., & Marzocchi, W. (2024). Illuminating the hierarchical segmentation of faults through an Unsupervised Learning Approach applied to clouds of earthquake hypocenters. *Earth and Space Science*, 11, e2023EA003267. <https://doi.org/10.1029/2023EA003267>

Received 28 AUG 2023

Accepted 1 MAY 2024

Author Contributions:

Conceptualization: E. Piegari, G. Camanni, W. Marzocchi
Formal analysis: E. Piegari, M. Mercurio
Investigation: E. Piegari, G. Camanni
Methodology: E. Piegari, G. Camanni, W. Marzocchi
Software: E. Piegari
Supervision: W. Marzocchi
Visualization: E. Piegari, M. Mercurio
Writing – original draft: E. Piegari
Writing – review & editing: E. Piegari, G. Camanni, M. Mercurio, W. Marzocchi

© 2024. The Author(s).

This is an open access article under the terms of the [Creative Commons Attribution-NonCommercial-NoDerivs License](#), which permits use and distribution in any medium, provided the original work is properly cited, the use is non-commercial and no modifications or adaptations are made.

Illuminating the Hierarchical Segmentation of Faults Through an Unsupervised Learning Approach Applied to Clouds of Earthquake Hypocenters

E. Piegari¹ , G. Camanni¹ , M. Mercurio¹, and W. Marzocchi¹

¹Dipartimento di Scienze della Terra, dell'Ambiente e delle Risorse, Università degli Studi di Napoli Federico II, Naples, Italy

Abstract We propose a workflow for the recognition of the hierarchical segmentation of faults through earthquake hypocenter clustering without prior information. Our approach combines density-based clustering algorithms (DBSCAN and OPTICS), and principal component analysis (PCA). Given a spatial distribution of earthquake hypocenters, DBSCAN identifies first-order clusters, representing regions with the highest density of connected seismic events. Within each first-order cluster, OPTICS further identifies nested higher-order clusters, providing information on their number and size. PCA analysis is applied to first- and higher-order clusters to evaluate eigenvalues, allowing discrimination between seismicity associated with planar features and distributed seismicity that remains uncategorized. The identified planes are then geometrically characterized in terms of their location and orientation in the space, length, and height. This automated procedure operates within two spatial scales: the largest scale corresponds to the longest pattern of approximately equally dense earthquake clouds, while the smallest scale relates to earthquake location errors. By applying PCA analysis, a planar feature outputted from a first-order cluster can be interpreted as a fault surface while planes outputted after OPTICS can be interpreted as fault segments comprised within the fault surface. The evenness between the orientation of illuminated fault surfaces and fault segments, and that of the nodal planes of earthquake focal mechanisms calculated along the same faults, corroborates this interpretation. Our workflow has been successfully applied to earthquake hypocenter distributions from various seismically active areas (Italy, Taiwan, and California) associated with faults exhibiting diverse kinematics.

Plain Language Summary Active faults are associated with ongoing movement and seismic activity. Recognizing them within large clouds of earthquake hypocenters is at the same time challenging and crucial for seismic hazard estimates. Here, we present a new procedure that can illuminate fault surfaces and its constituting segments by exclusively using hypocenter locations and their spatial density. We apply our approach to hypocenter distributions from various seismically active areas (Italy, Taiwan, and California). The evenness between the orientation of illuminated fault surfaces and fault segments, and that derived from other data sources, corroborates our workflow. This workflow is showed to be an effective tool to derive unbiased fault geometries. It also offers new perspectives for the study of the relationships between seismic activity patterns and fault segment interactions, as well as seismic forecasting.

1. Introduction

Geological faults, regardless their kinematics, only rarely occur as individual surfaces, but in most cases are complex structures comprising multiple fault segments (Camanni, Childs, et al., 2023; Camanni et al., 2019; Camanni, Freda, et al., 2023; Childs et al., 2009; Delogkos et al., 2020; Manighetti et al., 2009; Nicol et al., 2002; Roche et al., 2021; Walsh et al., 2003; Wesnousky, 1988). In seismically active areas, fault segmentation has been shown to have a significant impact on how a co-seismic rupture nucleates and propagates during an earthquake (Cesca et al., 2017; Hu et al., 2016; Li & Liu, 2020; Manighetti et al., 2007, 2009; Nissen et al., 2016; Perrin et al., 2016; Roche et al., 2022; Wesnousky, 1988, 2006). When an earthquake rupture progresses on a segmented fault and reaches a fault segment boundary, it can either stop propagating or jump to an adjacent segment, depending on the distance between adjacent segments (H. Wang et al., 2020; Wesnousky, 1988, 2006; Yıkılmaz et al., 2015). Consequently, a comprehensive knowledge of the segmentation of an active fault is fundamental for seismic hazard assessment and earthquake forecasting of an active region (Bello et al., 2022; Boncio et al., 2004; Chartier et al., 2019; Field et al., 2003; Martínez-Garzón et al., 2015; Woessner et al., 2015).

In seismically active areas, one approach that can be used for illuminating fault surfaces is by analyzing earthquake hypocenter spatial distributions (Brunsvik et al., 2021; Kamer et al., 2020; Kaven & Pollard, 2013; Ouillon & Sournette, 2011; Ouillon et al., 2008; Truttmann et al., 2023; Y. Wang et al., 2013). Associating earthquake hypocenters with fault surfaces is one of the most challenging open issues in seismic hazard assessment, especially for areas where auxiliary information from surface geology, borehole data and geophysical imaging is not available. In the last decades, several methods based on clustering algorithms have been proposed for achieving this. Partitional clustering such as k-means (Ouillon et al., 2008) and Gaussian Mixture models (Ouillon & Sournette, 2011) have been used to group earthquakes in clusters labeled as faults if the smallest principal component eigenvalue of every cluster is less than the earthquake location error. An attempt to introduce uncertainty of the spatial location of hypocenters using k-means clustering has been made by Y. Wang et al. (2013). Kamer et al. (2020) have proposed a sophisticated method for faults reconstruction based on agglomerative hierarchical clustering where faults are modeled by Gaussian kernels, which are merged until the information gain measured in terms of a Bayesian criterion is positive. Consecutive application of spectral clustering (Von Luxburg, 2007) and density-based clustering (Ester et al., 1996) have been used by Brunsvik et al. (2021) to reconstruct the main Paganica fault system activated during L'Aquila 2009 seismic sequence. An open-source toolbox built on density-based clustering has been provided by Petersen et al. (2021) to reconstruct the first-order geometry of faults. Furthermore, a density-based cluster analysis combined with earthquake ruptures, focal mechanisms and geological databases has been performed by Jian and Wang (2022) to reveal the extremely complex seismogenic structures related to the 2018–2022 Hualien earthquake sequence. A visual analysis approach that uses an algorithm based on singular value decomposition to fit planar surfaces has been developed by C. Wang et al. (2019). Truttmann et al. (2023) have introduced a method for 3D imaging of faults that combines nearest neighbor learning and principal component analysis (PCA) with a Monte Carlo-based approach to account for hypocenter relocation uncertainties.

While some of these studies focus on developing methods to also describe complex fault structures, they often do not fully address the hierarchical segmentation of the retrieved faults. The overarching goal of this work is to make this step forward by means of a new method for illuminating Hierarchical Segmentation of Faults through an Unsupervised Learning Approach (HSF-ULA).

Specifically, the HSF-ULA workflow is based on the combined use of two density-based clustering algorithms, DBSCAN (Ester et al., 1996) and OPTICS (Ankerst et al., 1999), and PCA (Pearson, 1901). Using in combination these clustering algorithms allows us to derive not only information on large-scale faults (through DBSCAN), but also, once they are defined, to derive the geometry of the fault segments comprised within it (through OPTICS).

Unlike previous approaches, where fault segment identification depends on operator-made assumptions (e.g., mechanically halving the cluster size (e.g., Ouillon et al., 2008) or assigning a probability to each data and assuming that the segments are well described by Gaussian kernels (e.g., Kamer et al., 2020; Ouillon & Sournette, 2011)), the new approach proposed here ensures that the fault segmentation hierarchy solely relies on the spatial density of the data.

The paper is organized as follows. In the next section, we describe the proposed workflow and provide details on how location, size and orientation of planar surfaces are retrieved. In Section 3, we apply the workflow to different areas (Italy, Taiwan, and California) where faults exhibit diverse kinematics (extensional, reverse, and strike-slip). For each case, a table with the results for first and second order planar surfaces is provided, while the results for the main third-order features are provided in Supporting Information S1. In Section 4, a comparison is made between the orientation of illuminated fault surfaces and that of the nodal planes of earthquake focal mechanisms calculated along the same faults. Finally, in Section 5 we discuss the obtained results and outline potential and limitations of the proposed procedure.

2. Methods

The proposed automated workflow is illustrated in Figure 1. To illuminate fault surfaces in a given earthquake hypocenter catalog, the first step consists in performing a cluster analysis by DBSCAN (Figure 1). The application of DBSCAN allows us to illuminate first-order clusters with the highest number of density-connected seismic events. This algorithm requires two inputs: ϵ , the neighborhood radius, and Z , the threshold minimum value for the number of points in the ϵ -neighborhood. Based on the values of ϵ and Z , DBSCAN groups together into clusters only density-connected hypocenters, that is, hypocenters whose neighborhoods contain at least Z

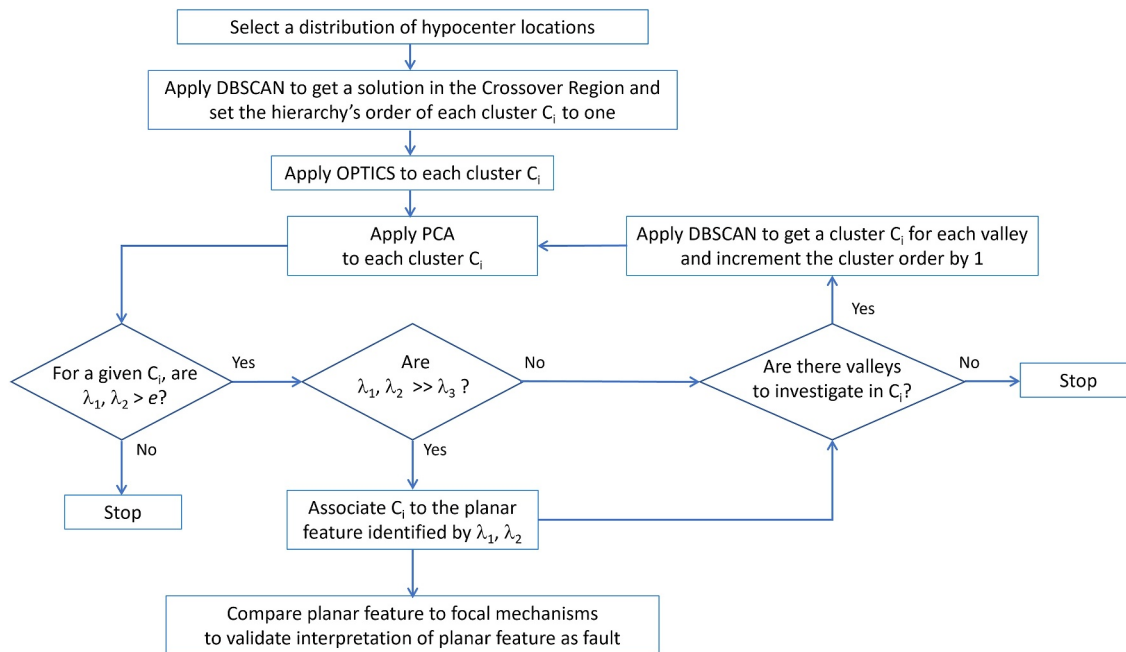


Figure 1. Flow diagram of the Hierarchical Segmentation of Faults through an Unsupervised Learning Approach workflow.

hypocenters that are in the ε -neighborhood of each other or lying on their boundaries; all the rest of hypocenters is considered noise and discarded from the cluster analysis. By varying ε and Z , DBSCAN provides a very large number of different solutions, which can be divided into five classes according to Piegari et al. (2022). We choose a solution in the class named Crossover Region (CR). This class includes the cluster solutions that simultaneously satisfy the two conditions: (a) number of noise points $<60\%$ and (b) number of points belonging to the biggest cluster $<60\%$. These solutions vary little in terms of number and size of the clusters and maximize the number of the largest clusters. This is the reason why we start by considering one of them, as it allows us to illuminate the biggest number of (first-order) clusters. We point out that the choice to start from an internal solution to the CR is determined solely by the preference to divide the data set into the greatest number of primary structures but does not affect the fault segmentation hierarchy, which is revealed by OPTICS (see below) and is dependent only on the spatial distribution of the data.

To define whether or not a first-order cluster can be associated to a planar feature, a PCA is performed (Figure 1). We note that, even if a data scaling is used to illuminate the biggest clusters and retrieve the cluster indices, PCA is applied to the original data set and not to the scaled data set. PCA is classified as an unsupervised machine learning algorithm for linear dimensionality reduction. It consists in diagonalizing the covariance matrix, that is, finding a new basis of coordinates aligned with the directions that maximize the data variation from the mean. The three eigenvalues λ_1 , λ_2 , and λ_3 correspond to the variance of the data in the new (decorrelated) reference system. Following Ouillon et al. (2008), if the two largest eigenvalues λ_1 and λ_2 are larger than location errors e directly extracted from data set and are much larger than the third one λ_3 , the cluster geometrically defines a planar feature (Figure 1). Within this cluster (or if the condition $\lambda_3 \ll \lambda_1, \lambda_2$ is not satisfied for the first-order cluster), the output of the algorithm OPTICS is then examined to investigate its internal hierarchy, for the identification of density-based, second-order, nested clusters (Figure 1).

The output of OPTICS is a type of graph called reachability plot, which visualizes the reachability distance of each point in the data set. Points belonging to a cluster have a low reachability distance to their nearest neighbor and are recognizable as valleys in the reachability plot. The deeper the valleys, the denser the clusters. Valleys are separated by peaks, which are points in the data set that are at relatively longer distances from their neighbors. Therefore, peaks in the reachability plot can be associated with transitions from one cluster to another and give information about the presence of different density regions within the data. Looking at the reachability plot, the choice of the valleys to investigate is made manually by setting a threshold on the y -axis that cuts off the valleys.

Then, second order clusters corresponding to such valleys are extracted by applying DBSCAN using the threshold as input value for ϵ .

PCA is iteratively applied to second-order clusters corresponding to each valley. For each of such second-order clusters, if the condition $\lambda_3 \ll \lambda_1, \lambda_2$ is satisfied, a planar feature is built. The reachability plot is then further inspected for the identification of third-order planar features within second-order ones, etc., up to the condition for planar geometry is not satisfied or the eigenvalues are smaller than location errors.

We emphasize that the only algorithm of the workflow that is computationally expensive is OPTICS. This is one of the reasons why we introduce its use only after the identification of the main first-order largest clusters is made. In this way, the initial amount of data is reduced by a percentage of noise data, which are discarded, and it is conveniently divided into subsets that are more easy to manage.

For characterizing the geometry of a recognized planar feature, the two eigenvectors \mathbf{u}_1 and \mathbf{u}_2 , corresponding to the eigenvalues λ_1 and λ_2 (i.e., the two principal components, determined by PCA) are used. The plane defining equation can be written in terms of the orthonormal eigenvector $\mathbf{u}_3 = \mathbf{n}$ related to the third eigenvalues λ_3 as:

$$\mathbf{n} \cdot \mathbf{x} - \mathbf{n} \cdot \boldsymbol{\mu}_C = 0,$$

where \mathbf{x} is a point that lie on the plane and $\boldsymbol{\mu}_C$ is the cluster barycenter. The third eigenvector \mathbf{n} can be also used to compute the strike (azimuth of a horizontal line lying on the plane) and dip (angle of maximum inclination of the plane) angles of the plane as follows (Quinn & Ehlmann, 2019):

$$\text{strike} = \tan^{-1} \frac{n_1}{n_2} - \frac{\pi}{2}$$

$$\text{dip} = \cos^{-1} \frac{n_3}{\|\mathbf{n}\|}$$

where n_1 , n_2 , and n_3 are the components of the vector \mathbf{n} . The dimensions (length and height) of the planes depend on data variability along the directions \mathbf{u}_1 and \mathbf{u}_2 and thus can be expressed as functions of λ_1 and λ_2 . According to Ouillon et al. (2008), for sake of simplicity we assume that hypocenter locations are uniformly distributed over the planes. If x is a 1D continuous random variable whose values are uniformly distributed on the interval $[a, b]$, its variance is given by:

$$\text{Var}(x) = \int_a^b (x - \mu)^2 \frac{1}{b-a} dx = \frac{(b-a)^2}{12}$$

where $\mu = (a + b)/2$. Generalizing this formula to a 2D case, it follows that an approximation for the length L and the height H of the fault planes can be obtained by the equations: $L = \sqrt{12\lambda_1}$, $H = \sqrt{12\lambda_2}$.

3. Application of HSF-ULA to Case Studies

3.1. Case 1: Clouds of Earthquake Hypocenters Associated With Extensional Faults (Italy)

As an example of application to a normal fault system, we test the developed workflow by illuminating planar surfaces within the hypocenter distribution of the 2009 L'Aquila (Italy) seismic sequence (Brunsvik et al., 2021; Chiaraluce, 2012; Lavecchia et al., 2012). We use the high-resolution earthquake catalog by Valoroso et al. (2013, 2020), which consists of 64,051 events spanning from 07 January 2009 to 20 December 2009.

In Figure 2a, it is shown a DBSCAN cluster solution in the CR corresponding to values of the input parameters $\epsilon = 0.5$ km and $Z = 200$. Note that before applying DBSCAN, we translated the horizontal coordinates to the hypocenter depth range (2.3–21.3 km) using the min-max scaling, which allowed us to consider the spatial anisotropy of the distribution (Piegari et al., 2022). The algorithm automatically illuminates six first-order clusters and discards about 12% of events classified as noise (gray points in Figure 2a). For brevity, we apply PCA only to the two largest first-order clusters (light blue and light green color points in Figure 2) related to L'Aquila and Campotosto faults (Brunsvik et al., 2021), respectively. The results of the applications of PCA with the

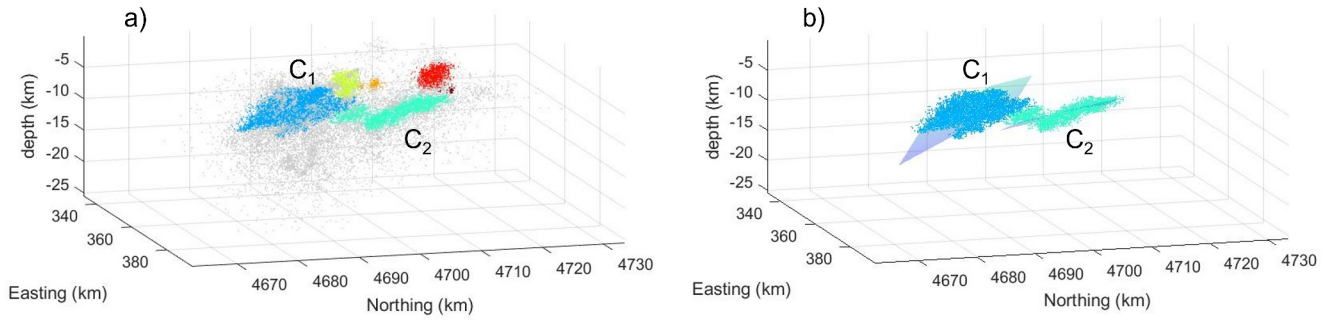


Figure 2. A workflow application to L'Aquila seismic sequence. (a) A DBSCAN solution illuminating six earthquake clusters ($Z = 200$ and $\epsilon = 0.5$ km). Gray points are earthquakes discarded as noise points. (b) First-order planar surfaces retrieved by principal component analysis are shown for the two biggest clusters C_1 and C_2 .

corresponding geometrical parameters for the reconstructed planar features are reported in Table 1, and the planes are illustrated in Figure 2b. In addition, to look for second-order clusters within C_1 and C_2 first-order-ones, OPTICS was applied. Results (Figure 3) show that several second-order clusters can be built within first-order ones. Note that all of them can be assigned a planar feature except the smallest second-order cluster C_{14} for which the condition $\lambda_3 \ll \lambda_1, \lambda_2$ is not satisfied. Looking at the reachability plots in Figures 3a and 3b, it is visible that many of the named valleys include other sub-valleys that can be associated to third-order clusters. The results of the investigation of the sub-clusters of C_{11} and C_{12} are reported in Supporting Information S1, along with the animated gif of the 3D plots in Figures 3c–3e.

3.2. Case 2: Clouds of Earthquake Hypocenters Associated With a Reverse Fault (Taiwan)

Seismicity of the active Taiwan mountain belt is associated with faults with varying kinematics (Kuoehen et al., 2004, 2007; Wu, Chang, et al., 2008; Wu, Zhao, et al., 2008). We apply the workflow to a spatial distribution of 87,679 earthquake hypocenters occurred in the period from 01 January 1990 to 31 December 2020 in the southeastern sector of the mountain belt (UTM coordinates from 265.99 to 377.5 km Easting and from 2,515.9 to 2,578.4 km Northing), in an area comprised within the Central and Coastal ranges of the mountain belt (Kuoehen et al., 2004, 2007).

Figure 4a shows a DBSCAN solution in the CR corresponding to $\epsilon = 1$ km and $Z = 80$. It has been obtained after scaling the horizontal coordinates to the hypocenter depth range (5–30 km) to take into account the spatial anisotropy of the distribution. This solution illuminates the biggest, first-order clusters C_1 and C_2 , respectively. We focus our analysis on C_2 as is it well-know from the literature that seismicity within it belongs to the Chihshang Fault, a reverse fault that was recently associated with the Mw 6.8 Chengkung earthquake occurred in

Table 1

Geometrical Parameters From Principal Component Analysis Applied to First-Order Clusters C_1 and C_2 in Figure 2 and Related Second-Order Clusters Shown in Figures 3c–3e

Cluster order	Symbol	N	Longitude (°)	Latitude (°)	Depth (km)	L (km)	H (km)	Dip (°)	Strike (°)	λ_3 (km ²)
I (L'Aquila Fault)	C_1	31,284	13.451	42.313	−5.7	25.2	8.4	38.9	144.4	0.6880
II (L'Aquila Fault)	C_{11}	18,988	13.497	42.285	−4.7	10.3	6.1	29.6	129.5	0.6356
	C_{12}	8,446	13.381	42.355	−7.6	10.4	5.4	49.4	140.4	0.1215
	C_{13}	1,291	13.291	42.418	−7.9	5.3	2.1	41.7	142.1	0.1340
	C_{14}	328	13.435	42.347	−3.4	–	–	–	–	0.1378
	I (Campotosto Fault)	C_2	11,634	13.371	42.469	−8.3	18.0	8.0	19.7	151.1
II (Campotosto Fault)	C_{21}	3,517	13.389	42.449	−9.2	10.4	2.8	25.0	144.5	0.1607
	C_{22}	2,871	13.380	42.493	−7.6	6.3	2.5	37.3	137.3	0.2068
	C_{23}	2,491	13.383	42.411	−8.2	5.7	2.3	34.7	139.5	0.1482
	C_{24}	2,080	13.324	42.532	−7.9	6.3	3.6	28.2	146.8	0.1572

Note. Longitude, Latitude, and Depth are those of the barycenter of the clusters.

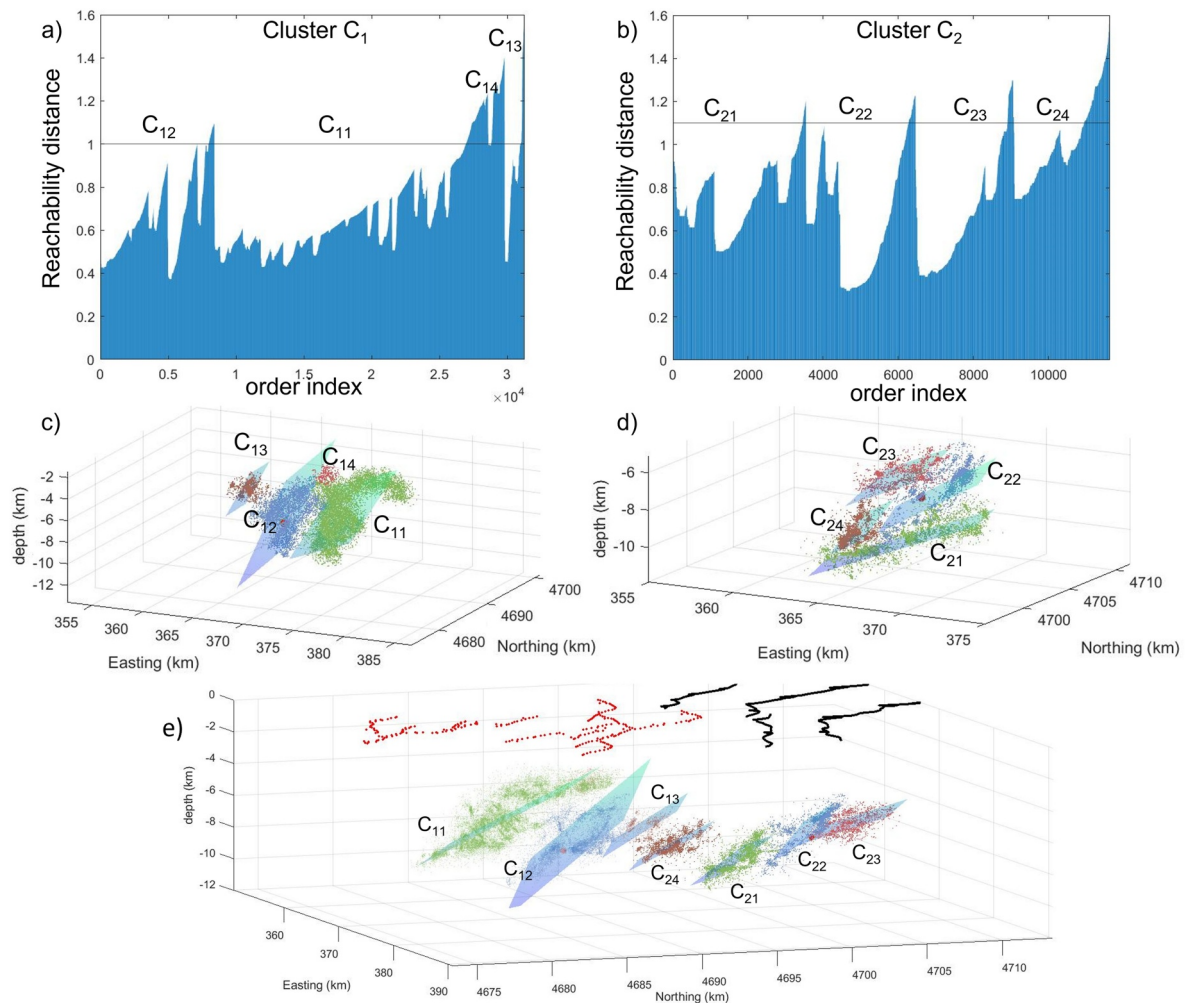


Figure 3. A workflow application to L'Aquila seismic sequence. In panels (a, b) reachability plot for clusters C_1 and C_2 of Figure 2, respectively. In panels (c, d) DBSCAN solutions for C_1 ($\epsilon = 1$ km and $Z = 200$) and C_2 ($\epsilon = 1$ km and $Z = 200$) with planar surfaces retrieved from principal component analysis, respectively. (e) A 3D view showing the seven second-order planes retrieved after two iterations of the procedure. The black and red traces at the surface correspond to the faults mapped at the surface in the L'Aquila area (Brunsvik et al., 2021). Earthquakes classified at each iteration as noise points are not shown.

2003 (Angelier et al., 2000; Ching et al., 2007; Kuochen et al., 2004, 2007; Mozziconacci et al., 2009). This cluster groups 16,244 earthquakes and can be associated to a first-order planar surface (see Figure 4b) defined by the parameters in Table 2. Figure 4c shows the reachability plot of C_2 , with the cut line $\epsilon = 2$ km that identifies the biggest valleys, that is, two main second-order clusters. Both of them can be associated to planar surfaces (see Figure 4d), whose parameters are reported in Table 3, and include several subvalleys. They are associated to third-order clusters and are investigated in Supporting Information S1.

3.3. Case 3: Clouds of Earthquake Hypocenters Associated With a Strike-Slip Fault (California, USA)

We apply the proposed methodology to the most recent swarm occurred in Cahuilla Valley (California, USA), in the area between the Elsinore and San Jacinto strike-slip faults (Cochran et al., 2023; Ross et al., 2020). The swarm seismicity is considered to be controlled by hot fluid circulation, which causes characteristic hypocenter migration patterns with a big number of earthquakes in a relatively small volume (Cochran et al., 2023; Hauksson et al., 2019; Ross et al., 2020). We use the high-resolution catalog available at Caltech (2020), which consists of 22,700 events spanning from 01 January 2016 to 28 June 2019.

Figure 5a shows a DBSCAN cluster solution with $\epsilon = 0.5$ km and $Z = 100$. The algorithm identifies six clusters and discards about 5% of events classified as noise (gray points in Figure 5a). We apply PCA only to the biggest

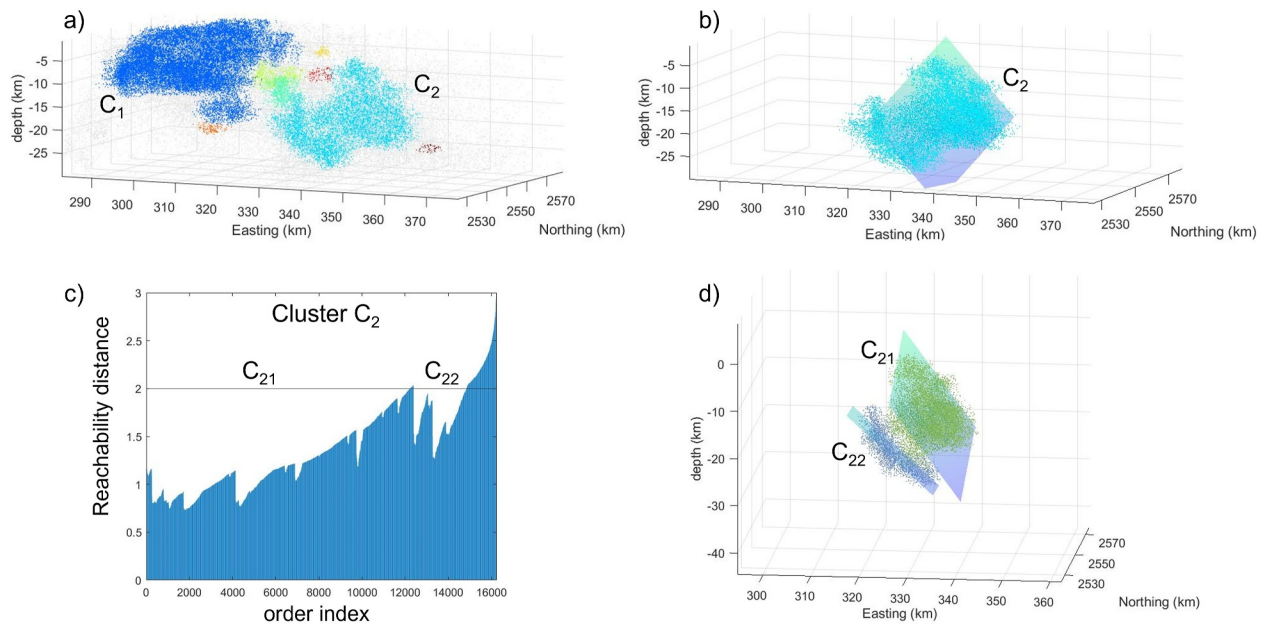


Figure 4. A workflow application to Taiwan data set. (a) A DBSCAN solution illuminating eight earthquake clusters in a southeastern sector of Taiwan ($Z = 80$ and $\epsilon = 1$ km). (b) First-order planar surface retrieved by principal component analysis (PCA) is shown for the biggest cluster C_2 . (c) Reachability plot of C_2 with the cut line $\epsilon = 2$ km. (d) DBSCAN solution ($\epsilon = 2$ km and $Z = 80$) with planar surfaces retrieved by PCA. Earthquakes classified as noise points are shown only in the first panel in gray color.

first-order cluster C_1 (see Figure 5b) containing nearly all earthquakes (19,621 events) and related to a strike-slip fault. Figure 5c shows the reachability plot of C_1 , with the cut line $\epsilon = 0.21$ km that identifies several valleys associated to second-order clusters. By applying PCA, we retrieved the geometrical parameters reported in Table 3. The covariance matrices of C_1 and C_{11} have the largest eigenvalues λ_1 and λ_2 of the order of about 1 km, that is, much larger than relative horizontal and vertical errors (38 and 87 m, respectively (Ross et al., 2020)). This is the reason why an estimate of the related planar surfaces is attempted even if in both cases the third eigenvalue λ_3 is less than the resolution error (see Table 3). Note that the third eigenvalues of all the remaining second-order clusters are much smaller than the resolution error. Therefore, the related seismicity stays uncategorized.

4. Comparison Between Calculated Planar Features and Fault Focal Mechanisms

In all areas, orientation of planes retrieved from PCA analysis on both first- and second-order clusters shows a good fit with that derived from nodal planes of focal mechanisms calculated for the same clusters (see Table 4). This suggests that the reconstructed planar features for the first-order clusters can be interpreted as fault surfaces, while those within second-order clusters as fault segments within the embedding fault surface.

Within the same first-order cluster, a planar feature output of PCA analysis before applying OPTICS can be interpreted as a fault surface with a thickness given by the square root of λ_3 , while planes output of PCA analysis after OPTICS can be interpreted as fault segments contained within the fault surface.

Table 2

Geometrical Parameters From Principal Component Analysis Applied to First-Order Cluster C_2 and Related Second-Order Clusters Shown in Figures 4b and 4d

Cluster order	Symbol	N	Longitude (°)	Latitude (°)	Depth (km)	L (km)	H (km)	Dip (°)	Strike (°)	λ_3 (km ²)
I (Chihshang Fault)	C_2	16,244	121.344	23.090	18.3	45.6	16.0	47.6	14.3	3.3626
II (Chihshang Fault)	C_{21}	12,227	121.353	23.140	17.9	27.4	15.0	54.3	14.9	1.8778
	C_{22}	2,463	121.305	22.894	19.6	18.0	12.5	42.5	2.3	2.5074

Note. Longitude, Latitude, and Depth are those of the barycenter of the clusters.

Table 3

Geometrical Parameters From Principal Component Analysis Applied to First-Order Cluster C_1 and Related Second-Order Clusters Shown in Figures 5b and 5d

Cluster order	Symbol	N	Longitude (°)	Latitude (°)	Depth (km)	L (km)	H (km)	Dip (°)	Strike (°)	λ_3 (km ²)
I (Cahuilla Fault)	C_1	19,621	-116.790	33.503	6.8	3.5	3.2	79.9	344	0.015
II (Cahuilla Fault)	C_{11}	14,108	-116.789	33.501	6.8	3.4	2.7	80.7	345	0.005
	C_{12}	950	-116.792	33.508	7.0	-	-	-	-	0.001
	C_{13}	737	-116.796	33.518	6.7	-	-	-	-	0.001
	C_{14}	501	-116.789	33.515	8.4	-	-	-	-	3.e-04
	C_{15}	356	-116.786	33.488	6.0	-	-	-	-	0.002

Note. Longitude, Latitude, and Depth are those of the barycenter of the clusters.

5. Discussion

We have presented a new methodology with a dual purpose of illuminating the main fault surfaces within hypocenter clouds and investigating the possible occurrence of a hierarchical segmentation within them. The results obtained for the L'Aquila seismic sequence show that starting from a DBSCAN solution in the CR allows us to naturally illuminate the main faults (L'Aquila Fault and Campotosto Fault) at the first step as first-order structures. Note that this output is found without the application of any data filter, that is, we used all data without reduction on magnitudes or spatial extension. The same consideration holds also for the Taiwan and Cahuilla data sets.

The Cahuilla data set is unique, with approximately 86% of the data concentrated in a relatively small area compared to other analyzed seismic sequences. For this reason, an initial choice of DBSCAN parameters was made just outside the CR, solely for the purpose of describing the densest area of hypocenters corresponding to the listric fault identified in the literature as the first-order cluster. In fact, based on how the CR is defined (Piegari et al., 2022), if the choice of parameters falls within the CR, the largest cluster must contain less than 60% of the

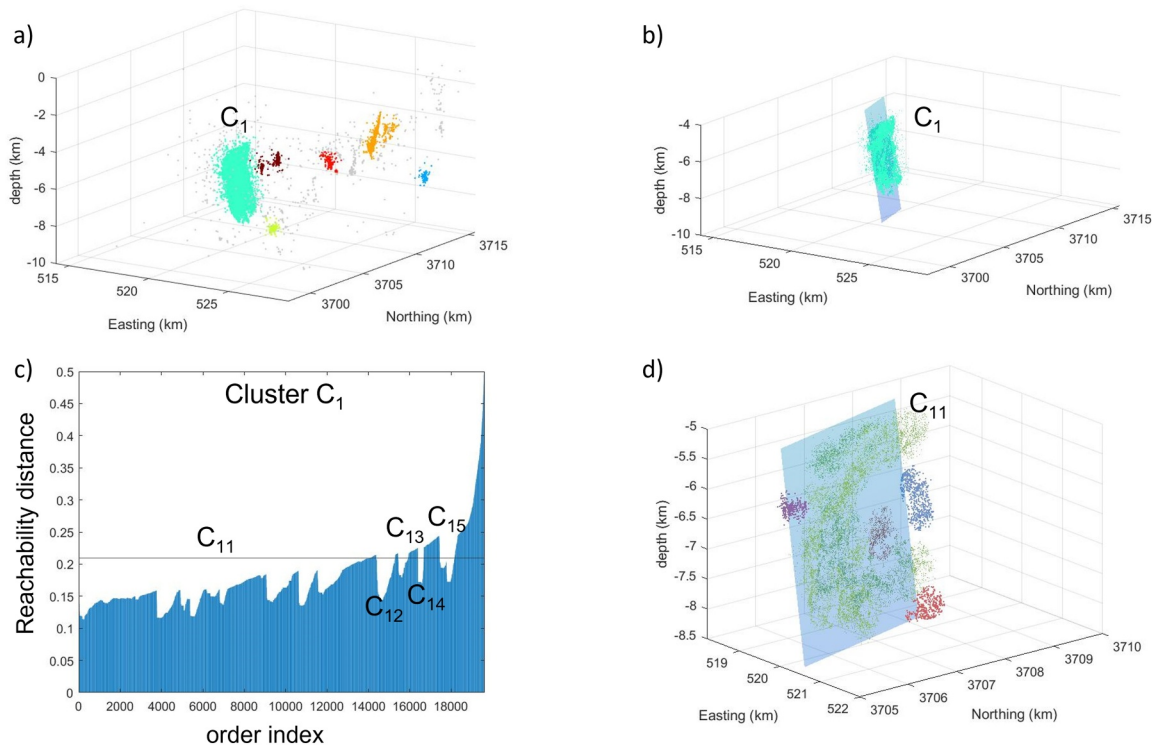


Figure 5. A workflow application to Cahuilla data set. (a) A DBSCAN solution illuminating six earthquake clusters in Cahuilla Valley ($Z = 100$ and $\epsilon = 0.5$ km). (b) First-order cluster C_1 with the planar surface retrieved by principal component analysis. (c) Reachability plot of C_1 with the cut line $\epsilon = 0.21$ km. (d) DBSCAN solution ($Z = 100$ and $\epsilon = 0.21$ km) with second-order clusters. Earthquakes classified as noise points are shown only in the first panel in gray color.

Table 4
Comparison Between the Estimated Fault Parameters and Those Retrieved by Focal Mechanisms

Case 1: extensional faults (Italy data set)						
L'Aquila Fault						
Fault angles	HSF-ULA (I-order)	HSF-ULA (II-order)	Brunsvik et al. (2021)	Lavecchia et al. (2012)	Chiaraluca (2012)	Boncio et al. (2010)
Dip (°)	~39	~30–49	~42.6	~45	~48	
Strike (°)	~N144	~N130–N142	~N143	~N140	~N137	N130–N140
Campotosto Fault						
Dip (°)	~20	~25–37		~50	~20	
Strike (°)	~N151	~N137–147	~N150	N140–150	~45–50	
Case 2: reverse faults (Taiwan data set)						
Chihshang fault						
Fault angles	HSF-ULA (I-order)	HSF-ULA (II-order)	Angelier et al. (2000)	Kuoehen et al. (2007)	Chen et al. (2008)	
Dip (°)	~48	~42–54	~39–45	~45	~45–50	
Strike (°)	~N14E	~N2–15E	~N18E	N36.5E		
Case 3: strike-slip faults (California data set)						
Cahuilla fault						
Fault angles	HSF-ULA (I-order)	HSF-ULA (II-order)	Ross et al. (2020)	Cochran et al. (2023)		
Dip (°)	~80	~81	~70/80	82		
Strike (°)	344	345	–	343		

data. However, we would like to clarify that if a choice of parameters had been made within the CR, the reachability plot would have still identified the same fault segments, and the only thing that would have changed is the order numbering. This means that for a solution in the CR the cluster C_{11} of Figure 5d would become the cluster C_1 keeping its shape essentially unchanged.

The reachability plots for the other two data sets show a more articulated spatial distribution of earthquakes. In particular, within the first-order Campotosto cluster, four second-order valleys are well evident. They show that the first-order structure is actually not a single surface but it is composed by four main planar segments with different dips that combined together give shape to a listric geometry, in accordance with what derived from other data sources (Chiaraluca et al., 2011). A curved surface also describes the large Chihshang fault (e.g., Kuoehen et al., 2007). In this case, the application of the proposed workflow allows us to identify two second-order planar segments with higher and lower dip angles in the northern and southern sectors, respectively. Looking at the reachability plot in Figure 4c, it is visible that both second-order surfaces are composed of other segments related to the relative sub-valleys. From the analysis of the main third-order clusters, which is reported in Supporting Information S1, a higher dip angle of about 50° is also found for the southern part of large first-order fault structure.

Looking at the reachability plot related to the cluster C_1 associated with L'Aquila fault, third order clusters are easily recognizable as valleys included in the second-order clusters C_{11} and C_{12} (see Figure 3a). The application of DBSCAN and PCA on such sub-valleys allows us to investigate the geometries of the associated faults in more detail (see Supporting Information S1). In particular, the analysis of the valleys of C_{11} shows that the complex morphology of the associated fault can be approximated by two distinct sets of planar segments describing two different types of seismicity: a shallower seismicity concentrated in an almost flat region characterized by very low dip angles (about 10°, see Supporting Information S1) and a deeper seismicity related to a fault segment with a vertical extension up to 10 km.

The identification of second and third order planar segments cannot be achieved by a single run of DBSCAN, but it requires the visual inspection of the reachability plots for the selection of the appropriate ϵ value. This is a limitation of the proposed approach, which at this stage is not fully automatic. However, once the choice of the valleys to

investigate is made by setting the ϵ value, the procedure is very simple, fast and reproducible, providing parameters and visualization of planar surfaces in a few minutes. Furthermore, the computation of the reachability plot is not dependent on the choice of input parameter values of DBSCAN, but rather reflects the data distribution in space, so the determination of the hierarchy of fault segments is not operator-dependent but solely based on the data.

A current limitation of the proposed approach is the manual selection of reachability thresholds to determine the valleys to investigate, which can introduce user bias and potentially affect the hierarchical order of fault segments. Indeed, a slight variation in the reachability threshold can lead to the merging or splitting of two valleys, resulting in a change of the hierarchical order. At present, the criterion used is to select a reachability distance threshold value that can identify the largest number of the largest (in terms of valley width) and well-confined (in terms of distance and depth) clusters. Although a full objectivity is unreachable, in future studies, we will refine the approach to make it fully automatic in the search for valleys to investigate, clarifying the rules adopted to achieve this goal.

Another limitation of the workflow is related to the use of Euclidean distance as the metric to compute the similarity between data. Since the UTM coordinate system uses map projections, a relative location error is introduced due to the Earth's curvature. Such an error is usually negligible if the investigated hypocenter distribution extends within the same UTM zone, as in the cases examined in the paper. A further element to improve the workflow is the introduction of uncertainty of attributing earthquakes to clusters. With the goal to keep the approach simple, the output of the presented workflow is an earthquake classification where each hypocenter is strictly assigned to a planar segment or belongs to uncategorized seismicity. Note that a percentage of earthquakes associated to first-order planar surfaces becomes uncategorized when second-order structures are investigated and the same happens when third or higher-order clusters are searched.

Overall, the workflow presented in this article has proven to be a valuable tool for roughly illuminating fault surfaces and their segmented nature. However, it is important to note here that this workflow, while providing valuable information for the degree of segmentation of a fault, has unavoidable limitations. For instance, the 3D shape of the tip lines (i.e., boundaries of a fault at which its displacement is null) bounding the automatically retrieved fault surfaces and segments are rectilinear and may differ from their actual shapes. Furthermore, the computation of planar surfaces has been conducted under the assumption of earthquakes uniformly distributing over the fault, which may lead to an inaccurate evaluation of fault length and width. Also, this workflow assumes that the entirety of a fault surface/segments is active, and therefore illuminated by earthquake hypocenters. However, this may not be the case and consequently the automatically retrieved faults may be incomplete surfaces. Therefore, it is essential to exercise caution when using these results. Instead, we recommend using them as proxies to further define fault geometries accurately, a task best carried out by a structural geologist familiar with the 3D geometrical templates of segmented faults, as well as with the geometrical peculiarities of faults of an area.

To end, we outline some perspectives for the future use of the workflow. The study of the spatio-temporal variations of the frequency-magnitude distributions related to the various clusters/segments can provide important implications for seismic hazard forecasting (Herrmann et al., 2022). Furthermore, by splitting the examined hypocenter distribution in different periods, co-seismic interactions between fault segments of different order could be investigated for tracking possible routes of 4D progression of ruptures during an earthquake.

6. Conclusions

We propose a methodology exclusively based on unsupervised machine learning algorithms to obtain an unbiased reconstruction of main faults and their hierarchical segmentation within clouds of earthquake hypocenters. We applied the method to seismic events occurred along faults with diverse kinematics and we were able to estimate fault parameters consistent with those already known by focal mechanisms.

The method allows the reconstruction of faults at multiple scales. The largest one depends on the specific hypocenter distribution and it is bound by the longest pattern of approximately equal dense regions of earthquakes. The lowest one is related to the resolution error.

The use of DBSCAN and OPTICS and the iterative loops of DBSCAN and PCA first allow the identification of the largest faults and then illuminate the related segments of decreasing sizes. The retrieved planar surfaces are not randomly oriented but have overall a very similar orientation to the fault orientation that can be derived from earthquake focal mechanisms calculated from the same earthquake clusters. The combined analysis of the

orientations, sizes, and spatial arrangements of the retrieved fault segments, by also taking into account the temporal dimension, is a promising way for investigating the 4D progression of ruptures during an earthquake, with important implications on short- and long-term hazard forecasting.

Conflict of Interest

The authors declare no conflicts of interest relevant to this study.

Data Availability Statement

L'Aquila seismic sequence data set is available at <https://doi.org/10.5281/zenodo.4036248> and Cahuilla data set is available at <https://scedc.caltech.edu/data/cahuilla-swarm.html>.

The three data sets used in this study are provided as Supporting Information S1 and are available at <https://doi.org/10.5281/zenodo.8210903> (Piegari et al., 2023b). The code to perform the cluster and principal component analyses is implemented in MATLAB environment and makes use of software packages available in the Statistics and Machine Learning Toolbox of MATLAB R2023a. It is permanently stored in the repository <https://doi.org/10.5281/zenodo.8211032> (Piegari et al., 2023a). It is also publicly available on Github under the GPL-3.0 license: https://github.com/epiegari/hypo_clustering.

Acknowledgments

We wish to thank two anonymous reviewers for their useful suggestions and comments, which definitely helped improving the manuscript. G. C. acknowledges Dennis Brown, Hao Kuo-Chen, and Vincent Roche for several discussions on the topic of this paper. This study was partially carried out within the RETURN Extended Partnership and received funding from the European Union Next-GenerationEU (National Recovery and Resilience Plan—NRRP, Mission 4, Component 2, Investment 1.3—D.D. 1243 2/8/2022, PE0000005).

References

- Angelier, J., Chu, H. T., Lee, J. C., & Hu, J. C. (2000). Active faulting and earthquake hazard: The case study of the Chihshang fault, Taiwan. *Journal of Geodynamics*, 29(3–5), 151–185. [https://doi.org/10.1016/S0264-3707\(99\)00045-9](https://doi.org/10.1016/S0264-3707(99)00045-9)
- Ankerst, M., Breunig, M. M., Kriegel, H. P., & Sander, J. (1999). OPTICS: Ordering points to identify the clustering structure. *ACM Sigmod Record*, 28(2), 49–60. <https://doi.org/10.1145/304181.304187>
- Bello, S., Lavecchia, G., Andrenacci, C., Ercoli, M., Cirillo, D., Carboni, F., et al. (2022). Complex trans-ridge normal faults controlling large earthquakes. *Scientific Reports*, 12(1), 10676. <https://doi.org/10.1038/s41598-022-14406-4>
- Boncio, P., Lavecchia, G., & Pace, B. (2004). Defining a model of 3D seismogenic sources for Seismic Hazard Assessment applications: The case of central Apennines (Italy). *Journal of Seismology*, 8(3), 407–425. <https://doi.org/10.1023/B:JOSE.0000038449.78801.05>
- Boncio, P., Pizzi, A., Brozzetti, F., Pomposo, G., Lavecchia, G., Di Naccio, D., & Ferrarini, F. (2010). Coseismic ground deformation of the 6 April 2009 L'Aquila earthquake (central Italy, Mw6. 3). *Geophysical Research Letters*, 37(6), L06308. <https://doi.org/10.1029/2010GL042807>
- Brunsvik, B., Morra, G., Cambiotti, G., Chiaraluce, L., Di Stefano, R., De Gori, P., & Yuen, D. A. (2021). Three-dimensional paganic fault morphology obtained from hypocenter clustering (L'Aquila 2009 seismic sequence, Central Italy). *Tectonophysics*, 804, 228756. <https://doi.org/10.1016/j.tecto.2021.228756>
- Caltech. (2020). Cahuilla swarm catalog (2016–2019). Retrieved from <https://scedc.caltech.edu/data/cahuilla-swarm.html>
- Camanni, G., Childs, C., Delogkos, E., Roche, V., Manzocchi, T., & Walsh, J. (2023). The role of antithetic faults in transferring displacement across contractional relay zones on normal faults. *Journal of Structural Geology*, 168, 104827. <https://doi.org/10.1016/j.jsg.2023.104827>
- Camanni, G., Freda, G., Delogkos, E., Nicol, A., & Childs, C. (2023). 3D geometry and displacement transfer of an oblique relay zone on outcropping normal faults. *Journal of Structural Geology*, 177, 105001. <https://doi.org/10.1016/j.jsg.2023.105001>
- Camanni, G., Roche, V., Childs, C., Manzocchi, T., Walsh, J., Conneally, J., et al. (2019). The three-dimensional geometry of relay zones within segmented normal faults. *Journal of Structural Geology*, 129, 103895. <https://doi.org/10.1016/j.jsg.2019.103895>
- Cesca, S., Zhang, Y., Mouslopoulou, V., Wang, R., Saul, J., Savage, M., et al. (2017). Complex rupture process of the Mw 7.8, 2016, Kaikoura earthquake, New Zealand, and its aftershock sequence. *Earth and Planetary Science Letters*, 478, 110–120. <https://doi.org/10.1016/j.epsl.2017.08.024>
- Chartier, T., Scotti, O., & Lyon-Caen, H. (2019). SHERIFS: Open-source code for computing earthquake rates in fault systems and constructing hazard models. *Seismological Research Letters*, 90, 1678–1688. <https://doi.org/10.1785/0220180332>
- Chen, K. H., Nadeau, R. M., & Rau, R. J. (2008). Characteristic repeating earthquakes in an arc-continent collision boundary zone: The Chihshang fault of eastern Taiwan. *Earth and Planetary Science Letters*, 276(3–4), 262–272. <https://doi.org/10.1016/j.epsl.2008.09.021>
- Chiaraluce, L. (2012). Unravelling the complexity of Apenninic extensional fault systems: A review of the 2009 L'Aquila earthquake (central Apennines, Italy). *Journal of Structural Geology*, 42, 2–18. <https://doi.org/10.1016/j.jsg.2012.06.007>
- Chiaraluce, L., Valoroso, L., Piccinini, D., Di Stefano, R., & De Gori, P. (2011). The anatomy of the 2009 L'Aquila normal fault system (central Italy) imaged by high resolution foreshock and aftershock locations. *Journal of Geophysical Research*, 116(B12), B12311. <https://doi.org/10.1029/2011jb008352>
- Childs, C., Manzocchi, T., Walsh, J. J., Bonson, C. G., Nicol, A., & Schöpfer, M. P. (2009). A geometric model of fault zone and fault rock thickness variations. *Journal of Structural Geology*, 31(2), 117–127. <https://doi.org/10.1016/j.jsg.2008.08.009>
- Ching, K. E., Rau, R. J., & Zeng, Y. (2007). Coseismic source model of the 2003 Mw 6.8 Chengkung earthquake, Taiwan, determined from GPS measurements. *Journal of Geophysical Research*, 112(B6), B06422. <https://doi.org/10.1029/2006JB004439>
- Cochran, E. S., Page, M. T., van der Elst, N. J., Ross, Z. E., & Trugman, D. T. (2023). Fault roughness at seismogenic depths and links to earthquake behavior. *The Seismic Record*, 3(1), 37–47. <https://doi.org/10.1785/0320220043>
- Delogkos, E., Manzocchi, T., Childs, C., Camanni, G., & Roche, V. (2020). The 3D structure of a normal fault from multiple outcrop observations. *Journal of Structural Geology*, 136, 104009. <https://doi.org/10.1144/SP439.19>
- Ester, M., Kriegel, H. P., Sander, J., & Xu, X. (1996). A density-based algorithm for discovering clusters in large spatial databases with noise. In *kdd* (Vol. 96, No. (34), pp. 226–231).
- Field, E. H., Jordan, T. H., & Cornell, C. A. (2003). OpenSHA: A developing community-modeling environment for seismic hazard analysis. *Seismological Research Letters*, 74(4), 406–419. <https://doi.org/10.1785/gssrl.74.4.406>

- Hauksson, E., Ross, Z. E., & Cochran, E. (2019). Slow-growing and extended-duration seismicity swarms: Reactivating joints or foliations in the Cahuilla valley Pluton, central Peninsular ranges, southern California. *Journal of Geophysical Research: Solid Earth*, *124*(4), 3933–3949. <https://doi.org/10.1029/2019JB017494>
- Herrmann, M., Piegari, E., & Marzocchi, W. (2022). Revealing the spatiotemporal complexity of the magnitude distribution and b-value during an earthquake sequence. *Nature Communications*, *13*(1), 5087. <https://doi.org/10.1038/s41467-022-32755-6>
- Hu, F., Zhang, Z., & Chen, X. (2016). Investigation of earthquake jump distance for strike-slip step overs based on 3-D dynamic rupture simulations in an elastic half-space. *Journal of Geophysical Research: Solid Earth*, *121*(2), 994–1006. <https://doi.org/10.1002/2015JB012696>
- Jian, P. R., & Wang, Y. (2022). Applying unsupervised machine-learning algorithms and MUSIC back-projection to characterize 2018–2022 Hualien earthquake sequence. *Terrestrial, Atmospheric and Oceanic Sciences*, *33*(1), 28. <https://doi.org/10.1007/s44195-022-00026-y>
- Kamer, Y., Ouillon, G., & Sornette, D. (2020). Fault network reconstruction using agglomerative clustering: Applications to south Californian seismicity. *Natural Hazards and Earth System Sciences Discussions*, *2020*, 1–23. <https://doi.org/10.5194/nhess-20-3611-2020>
- Kaven, J. O., & Pollard, D. D. (2013). Geometry of crustal faults: Identification from seismicity and implications for slip and stress transfer models. *Journal of Geophysical Research: Solid Earth*, *118*(9), 5058–5070. <https://doi.org/10.1002/jgrb.50356>
- Kuoehen, H., Wu, Y. M., Chang, C. H., Hu, J. C., & Chen, W. S. (2004). Relocation of eastern Taiwan earthquakes and tectonic implications. *Terrestrial, Atmospheric and Oceanic Sciences*, *15*(4), 647. [https://doi.org/10.3319/TAO.2004.15.4.647\(T\)](https://doi.org/10.3319/TAO.2004.15.4.647(T))
- Kuoehen, H., Wu, Y. M., Chen, Y. G., & Chen, R. Y. (2007). 2003 Mw6.8 Chengkung earthquake and its related seismogenic structures. *Journal of Asian Earth Sciences*, *31*(3), 332–339. <https://doi.org/10.1016/j.jseaes.2006.07.028>
- Lavecchia, G., Ferrarini, F., Brozzetti, F., De Nardis, R., Boncio, P., & Chiaraluce, L. (2012). From surface geology to aftershock analysis: Constraints on the geometry of the L'Aquila 2009 seismogenic fault system. *Italian Journal of Geosciences*, *131*(3), 330–347. <https://doi.org/10.3301/IJG.2012.24>
- Li, G., & Liu, Y. (2020). Earthquake rupture through a step-over fault system: An exploratory numerical study of the Leech River fault, southern Vancouver Island. *Journal of Geophysical Research: Solid Earth*, *125*(11), e2020JB020059. <https://doi.org/10.1029/2020JB020059>
- Manighetti, I., Campillo, M., Bouley, S., & Cotton, F. (2007). Earthquake scaling, fault segmentation, and structural maturity. *Earth and Planetary Science Letters*, *253*(3–4), 429–438. <https://doi.org/10.1016/j.epsl.2006.11.004>
- Manighetti, I., Zigone, D., Campillo, M., & Cotton, F. (2009). Self-similarity of the largest-scale segmentation of the faults: Implications for earthquake behavior. *Earth and Planetary Science Letters*, *288*(3–4), 370–381. <https://doi.org/10.1016/j.epsl.2009.09.040>
- Martínez-Garzón, P., Bohnhoff, M., Ben-Zion, Y., & Dresen, G. (2015). Scaling of maximum observed magnitudes with geometrical and stress properties of strike-slip faults. *Geophysical Research Letters*, *42*(23), 10230–10238. <https://doi.org/10.1002/2015GL066478>
- Mozziconacci, L., Delouis, B., Angelier, J., Hu, J. C., & Huang, B. S. (2009). Slip distribution on a thrust fault at a plate boundary: The 2003 Chengkung earthquake, Taiwan. *Geophysical Journal International*, *177*(2), 609–623. <https://doi.org/10.1111/j.1365-246X.2009.04097.x>
- Nicol, A., Gillespie, P. A., Childs, C., & Walsh, J. J. (2002). Relay zones between mesoscopic thrust faults in layered sedimentary sequences. *Journal of Structural Geology*, *24*(4), 709–727. [https://doi.org/10.1016/S0191-8141\(01\)00113-4](https://doi.org/10.1016/S0191-8141(01)00113-4)
- Nissen, E., Elliott, J. R., Sloan, R. A., Craig, T. J., Funning, G. J., Hutko, A., et al. (2016). Limitations of rupture forecasting exposed by instantaneously triggered earthquake doublet. *Nature Geoscience*, *9*(4), 330–336. <https://doi.org/10.1038/ngeo2653>
- Ouillon, G., Ducorbier, C., & Sornette, D. (2008). Automatic reconstruction of fault networks from seismicity catalogs: Three-dimensional optimal anisotropic dynamic clustering. *Journal of Geophysical Research*, *113*(B1), B01306. <https://doi.org/10.1029/2007JB005032>
- Ouillon, G., & Sourmette, D. (2011). Segmentation of fault networks determined from spatial clustering of earthquakes. *Journal of Geophysical Research*, *116*(B2), B02306. <https://doi.org/10.1029/2010JB007752>
- Pearson, K. (1901). LIII. On lines and planes of closest fit to systems of points in space. *The London, Edinburgh and Dublin Philosophical Magazine and Journal of Science*, *2*(11), 559–572. <https://doi.org/10.1080/14786440109462720>
- Perrin, C., Manighetti, I., Ampuero, J.-P., Cappa, F., & Gaudemer, Y. (2016). Location of largest earthquake slip and fast rupture controlled by along-strike change in fault structural maturity due to fault growth. *Journal of Geophysical Research: Solid Earth*, *121*(5), 3666–3685. <https://doi.org/10.1002/2015JB012671>
- Petersen, G. M., Niemi, P., Cesca, S., Mouslopoulou, V., & Bocchini, G. M. (2021). Clusty, the waveform-based network similarity clustering toolbox: Concept and application to image complex faulting offshore Zakynthos (Greece). *Geophysical Journal International*, *224*(3), 2044–2059. <https://doi.org/10.1093/gji/ggaa568>
- Piegari, E., Camanni, G., Mercurio, M., & Marzocchi, W. (2023a). hypo_clustering (hypo_clustering_software_v1.0) [Software]. Zenodo. <https://doi.org/10.5281/zenodo.8211032>
- Piegari, E., Camanni, G., Mercurio, M., & Marzocchi, W. (2023b). Illuminating the Hierarchical Segmentation of Faults through an Unsupervised Learning Approach applied to clouds of earthquake hypocenters (hypo_clustering_dataset_v1.0) [Dataset]. Zenodo. <https://doi.org/10.5281/zenodo.8210903>
- Piegari, E., Herrmann, M., & Marzocchi, W. (2022). 3-D spatial cluster analysis of seismic sequences through density-based algorithms. *Geophysical Journal International*, *230*(3), 2073–2088. <https://doi.org/10.1093/gji/ggac160>
- Quinn, D. P., & Ehlmann, B. L. (2019). A PCA-based framework for determining remotely sensed geological surface orientations and their statistical quality. *Earth and Space Science*, *6*(8), 1378–1408. <https://doi.org/10.1029/2018ea000416>
- Roche, V., Camanni, G., Childs, C., Manzocchi, T., Walsh, J., Conneally, J., et al. (2021). Variability in the three-dimensional geometry of segmented normal fault surfaces. *Earth-Science Reviews*, *216*, 103523. <https://doi.org/10.1016/j.earscirev.2021.103523>
- Roche, V., van der Baan, M., & Walsh, J. (2022). Examples of fault steps controlling event migration in seismic swarms. *SEG/AAPG International Meeting for Applied Geoscience & Energy*. <https://doi.org/10.1190/image2022-3738967.1>
- Ross, Z. E., Cochran, E. S., Trugman, D. T., & Smith, J. D. (2020). 3D fault architecture controls the dynamism of earthquake swarms. *Science*, *368*(6497), 1357–1361. <https://doi.org/10.1126/science.abb0779>
- Truttmann, S., Diehl, T., & Herwegh, M. (2023). Hypocenter-based 3D imaging of active faults: Method and applications in the southwestern Swiss Alps. *Journal of Geophysical Research: Solid Earth*, *128*(6), e2023JB026352. <https://doi.org/10.1029/2023JB026352>
- Valoroso, L., Chiaraluce, L., Piccinini, D., Di Stefano, R., Schaff, D., & Waldhauser, F. (2013). Radiography of a normal fault system by 64,000 high-precision earthquake locations: The 2009 L'Aquila (central Italy) case study. *Journal of Geophysical Research: Solid Earth*, *118*(3), 1156–1176. <https://doi.org/10.1002/jgrb.50130>
- Valoroso, L., Chiaraluce, L., Piccinini, D., Stefano, R., Schaff, D., & Waldhauser, F. (2020). The 2009 Mw 6.1 L'Aquila normal fault system imaged by 64,051 high-precision foreshock and aftershock locations (Version 1.0). Zenodo. <https://doi.org/10.5281/zenodo.4036248>
- Von Luxburg, U. (2007). A tutorial on spectral clustering. *Statistics and Computing*, *17*(4), 395–416. <https://doi.org/10.1007/s11222-007-9033-z>
- Walsh, J. J., Bailey, W. R., Childs, C., Nicol, A., & Bonson, C. G. (2003). Formation of segmented normal faults: A 3-D perspective. *Journal of Structural Geology*, *25*(8), 1251–1262. [https://doi.org/10.1016/S0191-8141\(02\)00161-X](https://doi.org/10.1016/S0191-8141(02)00161-X)

- Wang, C., Ke, J., Jiang, J., Lu, M., Xiu, W., Liu, P., & Li, Q. (2019). Visual analytics of aftershock point cloud data in complex fault systems. *Solid Earth*, *10*(4), 1397–1407. <https://doi.org/10.5194/se-10-1397-2019>
- Wang, H., Liu, M., Duan, B., & Cao, J. (2020). Rupture propagation along stepovers of strike-slip faults: Effects of initial stress and fault geometry. *Bulletin of the Seismological Society of America*, *110*(3), 1011–1024. <https://doi.org/10.1785/0120190233>
- Wang, Y., Ouillon, G., Woessner, J., Sornette, D., & Husen, S. (2013). Automatic reconstruction of fault networks from seismicity catalogs including location uncertainty. *Journal of Geophysical Research: Solid Earth*, *118*(11), 5956–5975. <https://doi.org/10.1002/2013JB010164>
- Wesnousky, S. (1988). Seismological and structural evolution of strike-slip faults. *Nature*, *335*(6188), 340–343. <https://doi.org/10.1038/335340a0>
- Wesnousky, S. (2006). Predicting the endpoints of earthquake ruptures. *Nature*, *444*(7117), 358–360. <https://doi.org/10.1038/nature05275>
- Woessner, J., Laurentiu, D., Laurentiu, D., Giardini, D., Crowley, H., Cotton, F., et al. (2015). The 2013 European seismic hazard model: Key components and results. *Bulletin of Earthquake Engineering*, *13*(12), 3553–3596. <https://doi.org/10.1007/s10518-015-9795-1>
- Wu, Y. M., Chang, C. H., Zhao, L., Teng, T. L., & Nakamura, M. (2008). A comprehensive relocation of earthquakes in Taiwan from 1991 to 2005. *Bulletin of the Seismological Society of America*, *98*(3), 1471–1481. <https://doi.org/10.1785/0120070166>
- Wu, Y. M., Zhao, L., Chang, C. H., & Hsu, Y. J. (2008). Focal-mechanism determination in Taiwan by genetic algorithm. *Bulletin of the Seismological Society of America*, *98*(2), 651–661. <https://doi.org/10.1785/0120070115>
- Yıkılmaz, M. B., Turcotte, D. L., Heien, E. M., Kellogg, L. H., & Rundle, J. B. (2015). Critical jump distance for propagating earthquake ruptures across step-overs. *Pure and Applied Geophysics*, *172*(8), 2195–2201. <https://doi.org/10.1007/s00024-014-0786-y>